Fabrication of rGO/cobalt-nickel oxide/polypyrrole composites and their electrochemical performance

YAN DONGXIAN[1], QIN LIN[1,*], FAN XIN[1,*], ZHANG XIAOHUI[2], PANG SHUHUA[1,2]
[1]*Guangxi Key Laboratory of Optical and Electronic Materials and Devices, Guangxi Colleges and Universities Key Laboratory of Natural and Biomedical Polymer Materials, College of Materials Science & Engineering, Guilin University of Technology, Guilin541004, PR China*
[2]*College of Materials & Chemical Engineering, Hezhou University, Hezhou 542899, PR China*

To meet people's requirements for high capacitance energy storage devices, the combination of two or even three materials with excellent properties enables electrode materials to have multiple mechanisms in electrochemical reaction at the same time, which improves electrochemical performance together. Herein, we have successfully synthesized rGO/metal oxide by Hummer's method and hydrothermal method and then further compounded with polypyrrole(PPy) by in-situ polymerization. The rGO/cobalt-nickel oxide/polypyrrole(rGO/NiCo/PPy) has a unique sea urchin-like structure coated with conductive polymer and its electrode displays large specific capacitance of 333.2 F/g at current density of 1 A/g. The ASC cell was assembled with rGO/NiCo/PPy as positive electrode and rGO/PPy as negative electrode. The specific capacitance of the ASC equipment attains up to 253 F/g at power density of 1250 W/kg. Then the specific capacitance remains 94% after 7000 charge and discharge cycles. Due to the escalation of specific surface area and the combination of bilayer capacitance with pseudocapacitance characteristics, the fundamental factors of the supervisor electrochemical characteristics are obtained. Furthermore, the asymmetric flexible supercapacitor equipment made of rGO/NiCo/PPy composite provides superior electrochemical performance.

1. Introduction

With industrial expansion, population growth and economic growth, energy demand is increasing. Traditional energy is not only limited, but also brings some environmental problems [1, 2]. Therefore, wind energy, tidal energy, solar energy and other renewable, clean and environmentally-friendly energy have aroused extensive research. The above energy needs to be stored and utilized in the form of electric energy before use, and supercapacitor devices is at the historic moment [3, 4] for converting and storing energy.

Supercapacitor has not only fast charging and discharging rate, good rate performance, long cycle life, but also high power density. On the other hand, compared to traditional capacitors and batteries, it is relatively safe and stable with lower maintenance costs [5, 6]. As the core material of supercapacitor, electrode materials directly determine the performance of supercapacitor such as carbon-based materials, metallic compounds and conductive polymers,

Carbon-based materials, such as activated carbon [7], carbon nanotubes (CNTs) [8], graphene [9], carbon fiber [10], graphite carbon and its composite materials [11], are widely used in supercapacitor due to its large surface area, excellent conductivity, high stability and good mechanical properties [12]. However, the electrode material based on

double electric layer has low capacitance and dense energy. This is a huge obstacle to its development in the field of energy storage. To increase the effective specific surface area of carbon materials is an effective method for improving the capacitance. Graphene with excellent physical and chemical stability, high specific surface area (theoretically up to 2630 m^2/g), high conductivity, high mechanical strength [13-15] acts as an energy storage device through a double layer of electrolyte ions on the surface of graphene. During the charge and discharge process, it benefits from the fact that cannot be limited by the electrochemical charge transfer kinetics, so it can obtain very high rate performance and cycle life. Therefore, graphene has received extensive attention and research. Guo et al [16] reported that an optimized 3D graphene skeleton could achieve an ultra-high height of 330 F/g in electrolyte.

Because of the merits of high specific capacitance and low resistance, metal oxide becomes another choice of electrode materials for supercapacitor, which makes it easier to manufacture high energy and high power supercapacitor [17]. They can provide higher energy densities in supercapacitor than conventional carbon materials, such as ruthenium oxide (RuO_x) [18], manganese oxide (MnO_x) [19,20], nickel oxide (NiO_x) [21], cobalt oxide (CoO_x) [22], iron oxide (FeO_x) [23], titanium oxide (TiO_2) [24], etc. Especially nickel and cobalt

oxide/hydroxide have become favorite electrode materials for supercapacitor due to their excellent theoretical capacitance, low preparation cost and environment-friendly property. For example, the theoretical capacitor values of nickel oxide, cobalt oxide and nickel hydroxide are 2584, 3560 and 2081 F/g, respectively [25, 26]. Although a single transition metal compound also has a huge theoretical capacitance, with the continuous expansion and deepening of pseudocapacitance, a single metal compound cannot meet the research needs, and people began to study the composite materials of different transition metal oxides and their compounds. Nickel-cobalt metal composite material can make use of the synergistic effect to obtain more excellent performance of the electrode material. When the binary Ni/Co metal is combined with different anions, it has better performances due to synergistic effect [27, 28]. Nickel-cobalt bimetallic oxides/hydroxides have a variety of oxidation states, such as Ni^{3+}/Ni^{2+}, $Co^{4+}/Co^{3+}/Co^{2+}$. Meanwhile, the conductivity of polymetallic oxides/hydroxides is higher than that of mono-metal oxides/hydroxides. The electrochemical properties of bimetallic nickel-cobalt based materials are not exactly the same as those of mono-metal nickel-cobalt based materials. The reversibility of bimetallic nickel-cobalt based materials is enhanced, as evidenced by the shape of cyclic voltammetry curves or reduced peak separation.

Conductive polymers, with low cost, can be synthesized by a simple method, and are easy to be modified by compounding with other materials [29]. In addition, their theoretical mass ratio is between carbon materials and metal oxides, generally much higher than carbon materials. Its energy storage mechanism is different from that of carbon materials and metal oxides, which is conducted by ion doping and dedoping processes. However, in these processes, the electrode material usually has serious volume expansion and shrinkage. Then the electrode material will powder off and the microstructure and the morphology will also change and result in shape collapse, leading to a sharp drop in capacity [30]. Common conductive polymers are polyaniline (PANI), polypyrrole (PPy), and poly(3,4)ethylene dioxythiophene (PEDOT) and corresponding derivatives [31-33]. PPy is one of the most important conductive polymer materials. Compared with PANI, although its theoretical mass specific capacity is slightly lower, PPy has excellent mechanical stability and is often used in flexible devices [34,35].

With the increasing demand for capacitance, the research of electrode materials is no longer limited to a single carbon electrode, transition metal electrode or conductive polymer electrode. The combination of two or even three materials enables electrode materials to have multiple mechanisms in electrochemical reaction at the same time, which improves electrochemical performance together. This method is mainly used to enhance the specific surface area and porosity of dual capacitance materials or the conductivity and morphology of pseudo-capacitance materials to improve the electrochemical performance of electrode materials, so that the electrode materials can accelerate the transfer of electrons and ion migration in the electrochemical process.

In this work, we use rGO as a conductive network supporting the redox reaction of transition metal oxides, hydroxides and conductive polymers to overcome the inherent poor electrical conductivity of nickel-cobalt oxide and PPy, as well as the inevitable volume shrinkage and expansion during the charging and discharging process which results the disadvantages of poor rate performance and low cycle stability in the practical application of supercapacitor. As we expected, the specific capacitance of rGO/NiCo/PPy is 333.2 F/g at 1 A/g. The asymmetric flexible device can achieve a specific capacitance of 253 F/g at 5A/g, and the specific capacitance after 7000 charge and discharge cycles still remains 94%.

2. Experimental

2.1. Synthesis of materials

The rGO/nickel oxide, rGO/cobalt oxide, and rGO/cobalt-nickel oxide was synthesized by hydrothermal synthesis method. Firstly, GO was prepared by Hummer's method, then 70 mg GO which was dispersed in 35 mL water was poured into beakers marked 1,2,3 respectively and sonicated for 40 minutes. Secondly, in beaker 1, 2.5 mmol nickel nitrate hexahydrate, 5 mmol cobalt chloride hexahydrate and 9 mmol urea were added into GO dispersion. In beaker 2, 2.5 mmol nickel nitrate hexahydrate and 9 mmol urea were poured into GO dispersion. In beaker 3, 5 mmol cobalt chloride hexahydrate and 9 mmol urea were put into GO dispersion. After stirring for 80 min with an invariable speed at normal temperature and then transferring to a 100 ml reaction still, the solution was reacted at 130 °C for 8 h in oven and cooled naturally to appropriate temperature. The mixture was washed with water and ethanol for several times until the filtrate became colorless and the filter residue was gathered. Then the residue was annealed at 350 °C with 3 °C/min of heating rate in natural conditions after drying at 80 °C for 15 h. Technically speaking final products in beakers 1, 2 and 3 was labeled as rGO/NiCo, rGO/Ni, and rGO/Co, respectively.

To compound polypyrrole, we performed the following operations: the purified pyrrole monomer was acidified and stirred at 0°C, then mixed with the prepared samples and slowly stirred in the ice bath for 1 h. Then the APS buffer was added into the solution drop by drop and stirred tardily for 1 h under the same conditions. The products were washed with distilled water and ethanol for several times after polymerizating successfully at low temperatures. Finally, the residue was placed at 70 °C for one night and the PPy-coated composites were obtained. Technically speaking final products in beakers 1, 2 and 3 was labeled as rGO/NiCo/PPy, rGO/Ni/PPy, and rGO/Co/PPy, respectively.

2.2. Characterization and electrochemical tests

The morphology images of the rGO/Ni, rGO/Co, rGO/NiCo, rGO/Ni/PPy, rGO/Co/PPy and rGO/NiCo/PPy composites were investigated by field-emission scanning

electron microscopy (FE-SEM, S-4800). X-ray diffraction (XRD) spectra were tested by PANalytical X'Pert Pro X-ray diffractometer which its 2θ range from 5 to 80° to get the crystal structures' analysis. Raman (Horiba JobinYvon) and FTIR (Nicolet Impact 400) were used to investigate the further structures, compositions and chemical bonding states of the obtained samples. The electrochemical properties of these sample and rGO/NiCo/PPy ASC device were tested on electrochemical workstation (CHI660E) by cyclic voltammetry (CV), galvanostatic charge/ discharge (GCD), electrochemical impedance spectroscopy (EIS) and charge-discharge cycling stability. The three-electrode test is operated in 3M KOH as followed: Pt foil is used as counter electrode and Hg/HgO electrode as reference electrode. For two-electrode system, the same test conducted on rGO/NiCo/PPy ASC device in 3 M KOH.

Specific capacitance (C_g, F/g) was calculated from the charge-discharge curves:

$$Cg = \frac{I \Delta t}{\Delta V \times m} \qquad (1)$$

where I is the discharge current density (A), Δt is the discharge time (s), m is the mass of active material (g), and ΔV is the potential window of a single electrode (V).

The two electrodes must conform to the principle that the positive and negative charges are equal, that is $q^+ = q^-$. We can calculate the appropriate mass ratio between each electrode via the following equation 2:

$$\frac{m_+}{m_-} = \frac{C_- \times \Delta V_-}{C_+ \times \Delta V_+} \qquad (2)$$

where C_+ and C_- (F/g) are the specific capacities of the rGO/NiCo/PPy and rGO/PPy electrodes, respectively, m (g) and ΔV (V) are the active material mass of each electrode and the potential window of ASC device, respectively. We fabricate the rGO/PPy materials as the anode electrode and the prepared rGO/NiCo/PPy as another electrode to assemble ASC device in 3 M KOH solution.

3. Results and discussion

3.1. Morphology characterization

The SEM images of rGO/Ni, rGO/Co, rGO/NiCo, rGO/Ni/PPy, rGO/Co/PPy and rGO/NiCo/PPy were shown in Fig. 1. As shown in Fig. 1a, the thin petals were closely connected and stacked close to each other into a ball, and the spherical objects were stacked on top of each other. Ni oxide with different sizes covered the surface of GO, indicating that the reduced graphene was well compounded with Ni oxide after reduction, forming a tight composite material. This good structure provides charge transfer and increases the contact area. This may be the reason that the positively charged Ni^{2+} closely bound with the negatively charged oxygen-containing functional groups on the surface of rGO through interaction and coordination, and formed Ni oxide. Compared with rGO/Ni, the morphology of rGO/Co in Fig. 1b had significantly changed into a "new Lamarck" flower-like structure or also called sea urchin-like structure, and micron-scale needle-rod like substance grown on the surface of the sphere. When nickel chloride and cobalt chloride was hydrothermal heated with GO at the same time, the SEM image of the resulting rGO/NoCo sample was shown in Fig. 1c. It can be seen that the morphology was integrated compared with Fig. 1a-b, and the micron-scale needle-rod material grown on the surface of the sea urchin sphere became softer and the rod became finer. Fig. 1d~1f showed the polymerization of PPy on rGO/Ni, rGO/Co, and rGO/NiCo, respectively. It can be seen that small PPy particles were uniformly attached to the sea urchin-like sphere.
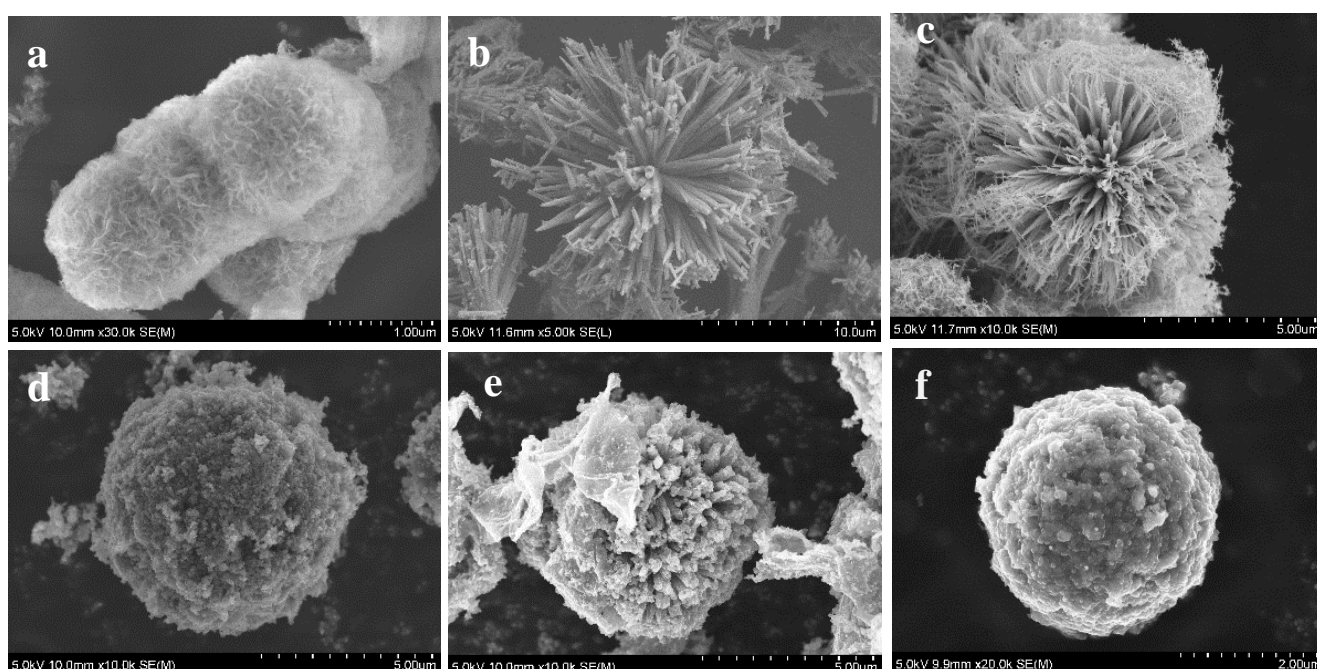
Fig. 1. SEM images of rGO/Ni (a), rGO/Co (b), rGO/NiCo (c), rGO/Ni/PPy(d), rGO/Co/PPy (e) and rGO/NiCo/PPy (f)

Fig. 2 was the EDX of rGO/NiCo/PPy. It can be clearly seen that carbon, nitrogen, oxygen, nickel and cobalt elements were evenly distributed on the sphere, indicating that the synthesis of the PPy was successful.
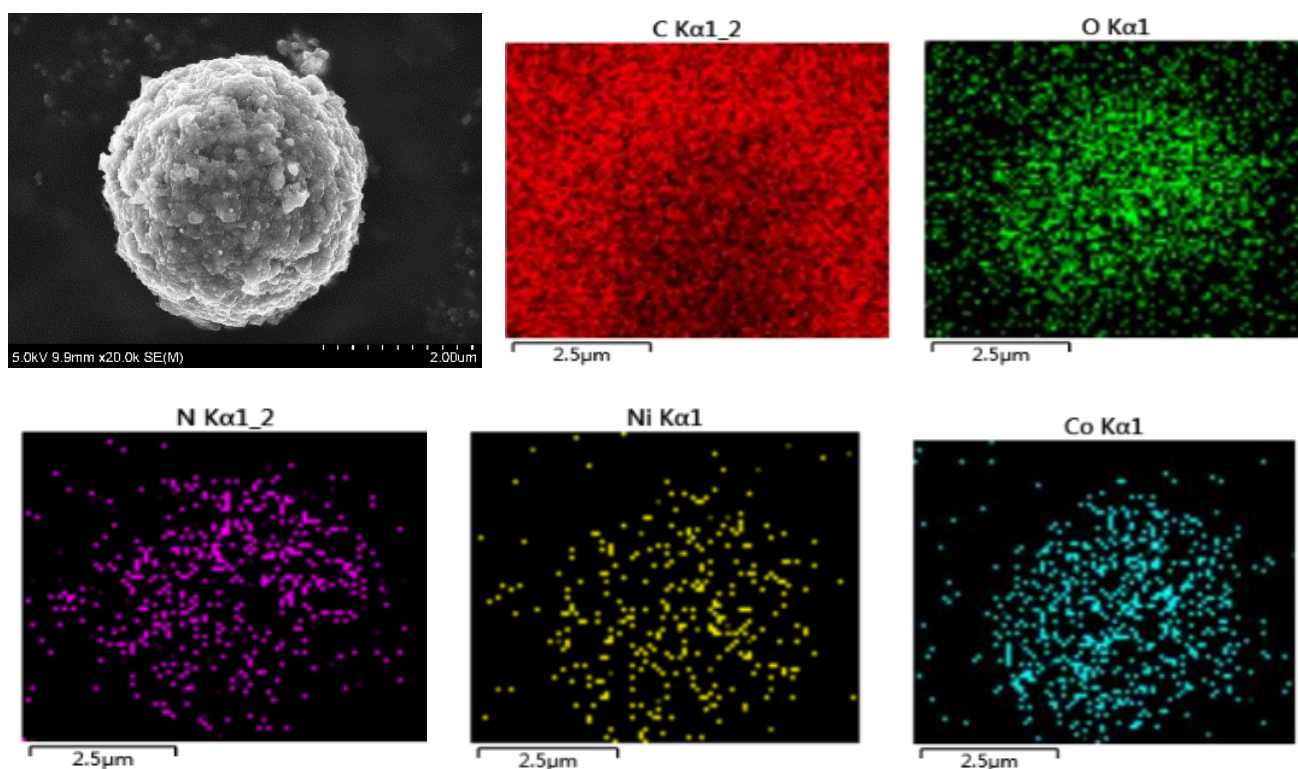
Fig. 2. EDX mapping of C, O, N, Ni and Co in rGO/NiCo/PPy (color online)

3.2. Structure of samples

The typical XRD patterns of rGO/Ni, rGO/Co, rGO/NiCo, rGO/Ni/PPy, rGO/Co/PPy and rGO/NiCo/PPy were shown in Fig. 3a. The diffraction peaks around at 18.89, 31.18, 36.61, 38.18, 44.58, 59.09 and 64.95° were corresponded to (111), (220), (311), (222), (400), (511) and (440) diffraction planes, respectively. These diffraction peaks can be attributed to cubic spinel $NiCo_2O_4$ structure (JCPDs card no. 20-0781) [36]. Due to the absence of others, the characteristic diffraction patterns corroborated the presence of highly purified $NiCo_2O_4$. The other materials also had the identical diffraction peaks of NiCo oxide, indicating the existence of NiCo oxide in other samples. It was also noted that for polypyrrole and rGO composites, wide diffraction peaks were observed near the 8-14° region, and the presence of these plate peaks distinctly indicated the amorphous characteristic of PPy. On the other hand, the diffraction peak at 25° was weak or didn't display, it may be due to the stacking of rGO sheets [37].

FT-IR spectra of rGO/Ni, rGO/Co, rGO/NiCo, rGO/Ni/PPy, rGO/Co/PPy and rGO/NiCo/PPy composites were shown in Fig. 3b. Due to the presence of water in the sample, the characteristic bands at 3389 and 1621 cm^{-1} were designated as O-H stretching and bending vibrations. The absorption peak of hydroxyl (-OH) in water was located at 1646 cm^{-1} and the stretching vibration peak of C-O was located near 1161 cm^{-1} [38]. For NiCo-containing elements, different tensile bands were shown at 1383, 650, and 554 cm^{-1}. Furthermore, the vibration of the tetrahedral cation (Td) produces 2345 cm^{-1} band and the asymmetrical stretching oscillation of Oh-O-Td correlated with 1383 cm^{-1} band. The metal-oxygen oscillations [39] were related to 650 and 554 cm^{-1} absorption bands that indicated the presence of nickel-cobalt metal elements in the compound. It was further observed that rGO/Ni/PPy, rGO/Co/PPy and rGO/NiCo/PPy samples displayed the specific bands of PPy at 1540 cm^{-1}, which is the characteristic peak of C-C bond in the pyrrole ring, and the band at 1450 cm^{-1} is the C-N bond in the pyrrole ring. The characteristic peaks at 3500 cm^{-1} corresponded to the N-H bond of the composite. In addition, the characteristic peaks at 966 cm^{-1} and 773 cm^{-1} confirmed the presence of PPy [40], and the characteristic peaks at 1187 and 905 cm^{-1} indicated that PPy and rGO were in a doping state.

Fig. 3c exhibited the Raman spectra of rGO/Ni/PPy, rGO/Co/PPy and rGO/NiCo/PPy nanocomposites. Referring to the literature [41], we can know that the characteristic peaks of Ni-Co metal were about 191, 464, 517 and 662 cm^{-1}, which are related to the classical vibration modes of F_{2g}, E_g and A_{1g} of NiCo spine structure, respectively. The characteristic peak was also observed in the whole nanocomposite, and the peak position was slightly offset. For all nanocomposites, two plate vibration bands were shown at approximately 1364 and 1590 cm^{-1}

due to the existence of the D-band and G-band of the reduced GO [42]. In general, the D-band represents structural disturbances such as defects in graphite domains while the G-band corresponds to E_{2g} pattern in sp^2 carbon territories. The ratio of D-band to G-band indicated the degree of graphitization. The presence of such bands evidently proved the existence of rGO in NiCo compounds. At the same time, small but distinct peaks were noticed at 981 and 937 cm^{-1}, which are related to the quinone type bipolaron and polaron structure of the PPy chain. The distinctive peak at 1054 cm^{-1} is related to the C-H deformation in the plane.
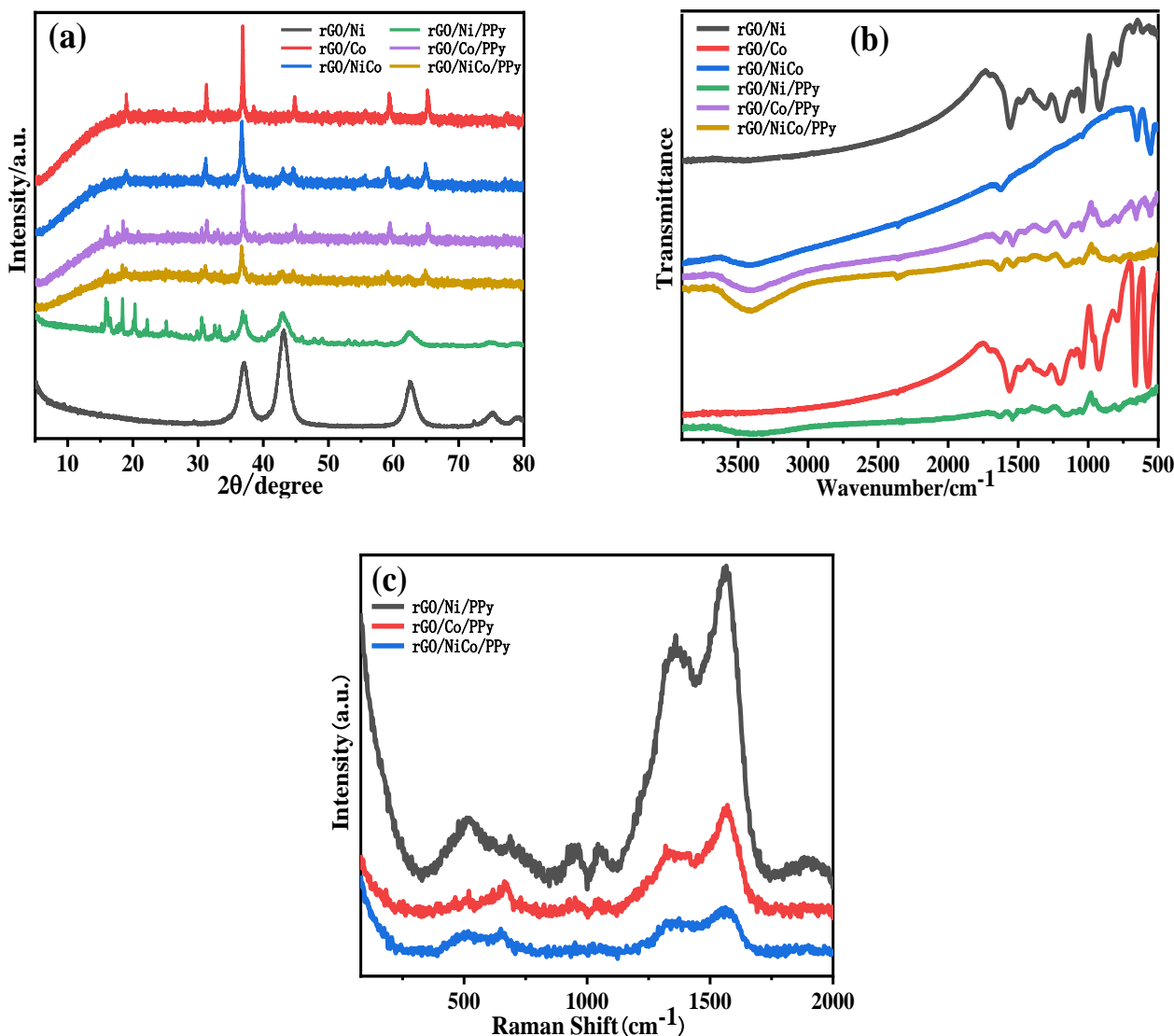
Fig. 3. XRD patterns (a), FT-IR spectra (b) and Raman spectra
(c) of rGO/Ni, rGO/Co, rGO/NiCo, rGO/Ni/PPy, rGO/Co/PPy and rGO/NiCo/PPy (color online)

3.3. Electrochemical properties

The electrochemical properties of rGO/Ni, rGO/Co, rGO/NiCo, rGO/Ni/PPy, rGO/Co/PPy and rGO/NiCo/PPy nanocomposite materials were performed by the CV, GCD and EIS.

Fig. 4 showed rGO/Ni, rGO/Co, rGO/NiCo, rGO/Ni/PPy, rGO/Co/PPy and rGO/NiCo/PPy composites in 0 to 0.5 V of potential window at 200 mV/s of scan rate All the electrode samples possessed a couple of redox peaks, manifesting pseudocapacitance behavior due to the presence of nickel and cobalt [43].
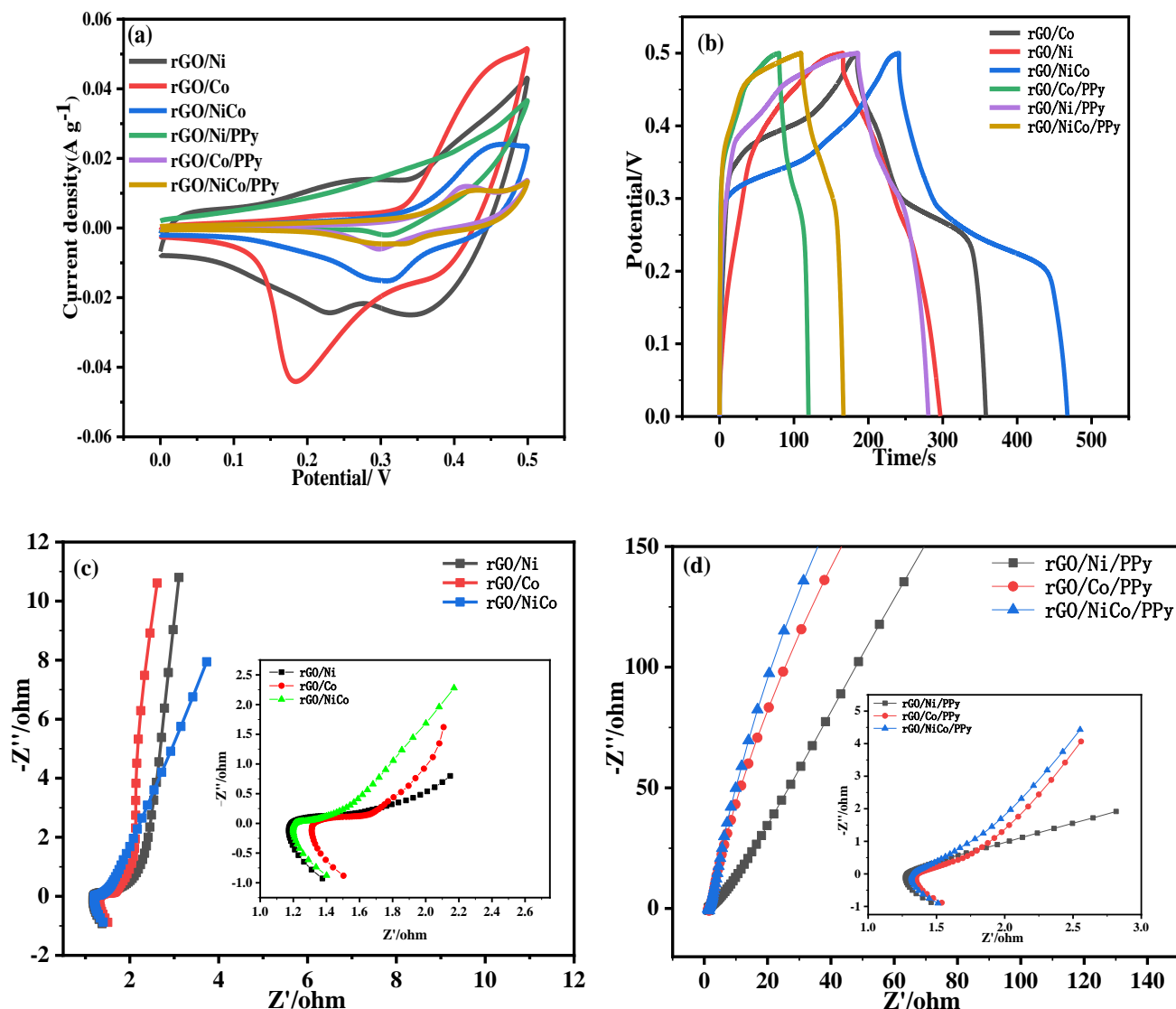
Fig. 4. Electrochemical performances of the samples: (a) CV at 200 mV/s and (b) GCD at 1 A/g, EIS of (c) Nickel-cobalt compounds (the inset shows the enlarged part of Nyquist plots) and (d) PPy-coated Nickel-cobalt compounds (color online)

Fig. 4 showed rGO/Ni, rGO/Co, rGO/NiCo, rGO/Ni/PPy, rGO/Co/PPy and rGO/NiCo/PPy composites in 0 to 0.5 V of potential window at 200 mV/s of scan rate All the electrode samples possessed a couple of redox peaks, manifesting pseudocapacitance behavior due to the presence of nickel and cobalt [43].

GCD is a basic procedure to analyze the electrochemical performance of electrode materials. In the potential range of 0 to 0.5 V, the GCD curves of the rGO/Ni, rGO/Co, rGO/NiCo, rGO/Ni/PPy, rGO/Co/PPy and rGO/NiCo/PPy at current density of 1 A/g were shown in Fig. 4b. The platform area and several voltage drops can be observed from the GCD. The results indicated that there exists pseudocapacitance behavior in composites. For these electrodes, the first potential drop is resulted from EDLC capacitor, while the second potential decreased with a broad discharge time stage is related to the coefficient of the EDLC and pseudocapacitance. GCD curve showed that rGO/NiCo had the longest discharge time and the largest specific capacitance in all electrodes. For all electrodes, the specific capacitance values were calculated by the Formula (1), and the specific capacitances of rGO/Ni, rGO/Co, rGO/NiCo, rGO/Ni/PPy, rGO/Co/PPy and rGO/NiCo/PPy were 716, 593.8, 935.2, 239.2, 561.4, 333.2 F/g, respectively. It is noteworthy that the specific capacitance of rGO/NiCo was improved to a certain extent due to the addition of rGO. The formation of unique sea urchin shape in rGO/NiCo may be its higher specific capacitance. However, after compounding pyrrole monomer, the sea urchin-like structure was reshaped, and the conductive polymer uniformly covered the sea urchin-like structure. Under the condition of alkaline electrolyte, the pseudocapacitance of metal oxides was hindered and the capacitance value was reduced.
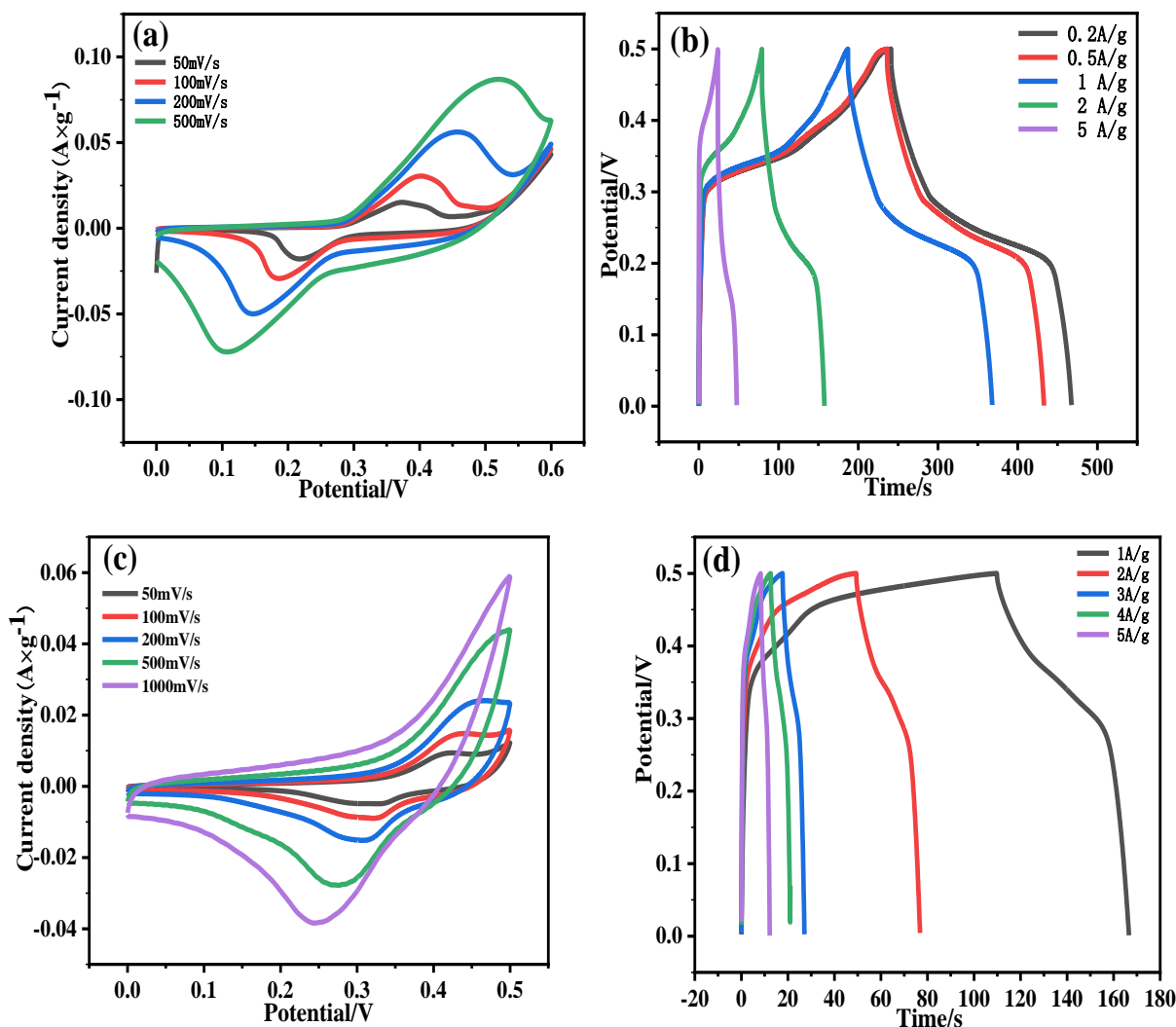
Fig. 5. (a) CV of rGO/NiCo electrode, (b) GCD of rGO/NiCo electrode, (c) CV of rGO/NiCo/PPy electrode, (d) GCD of rGO/NiCo electrode (color online)

Fig. 4c showed the EIS analysis of rGO/Ni, rGO/Co and rGO/NiCo in the frequency range of 0.01-10^5 Hz. The high frequency region is approximately a semicircular shape, and the intersection of EIS diagram and X axis represents the resistance of R_s [44], which includes the internal resistance of electrode material, electrolyte resistance and interface resistance. The values of R_s were approximately 1.4, 1.5 and 1.6, respectively. However, the low frequency region was approximately a straight line, indicating that the charge transfer resistance in the sample was very small. Fig. 4d was EIS diagram of rGO/Ni/PPy, rGO/Co/PPy and rGO/NiCo/PPy in the frequency range of 0.01-10^5Hz. Compared with Fig. 4c, PPy was passivated by alkaline electrolyte due to the addition of polypyrrole. Meanwhile, PPy was coated on the surface of metal oxide, which reduced the contact area between metal oxide and electrolyte and hindered pseudocapacitance behavior [45,46]. Therefore, R_s in Fig. 4d generally increased and was approximately 1.7. In the low-frequency region, the line originally biased towards the Y-axis also deviated from

the Y-axis, which also indicated that the charge transfer resistance of the composite increased after the polymerization of PPy.

CV and GCD analysis were performed on rGO/NiCo and rGO/NiCo/PPy composites, respectively. Fig. 5a revealed that rGO/NiCo had a clear redox peak, showing good pseudocapacitance performance. As the scanning rate increased, the redox peak shifted to a bigger potential value, which meant exceptional capacitance performance with excellent ionic response. Compared with other electrodes, the rGO/NiCo showed the highest integral value of the CV curve, indicating that the specific capacitance of the nanocomposites was enhanced. This may be due to the pseudocapacitance of NiCo and the double-layer capacitance of rGO. The specific capacitance of rGO/NiCo was the result of consolidation Faraday capacitance effect with double layer capacitance [47]. However, the nanocomposite containing PPy was dedoped due to deprotonation under alkaline conditions, and the exchange of pair anions and hydroxide ions in the doped film

destroyed the large conjugate structure of the polymer, resulting in the decrease of electrical conductivity. Meanwhile, PPy particles coated on rGO/Ni, rGO/Co and rGO/NiCo hindered the pseudocapacitive behavior of metal oxides.

Fig. 5c was the CV diagram of rGO/NiCo/PPy. Compared with rGO/NiCo, the pseudocapacitance behavior was weakened due to the double electric layer behavior of PPy, and the redox peak was not obvious, which showed that the integral area of CV curve decreased correspondingly, which was also consistent with the result in Fig. 5a.

Figs. 5b and 5d showed the GCD diagrams of rGO/NiCo and rGO/NiCo/PPy, respectively. It can be seen that both of them had large charge-discharge platforms and obvious voltage drops. More discharge time of rGO/NiCo pointed out that it had enormous specific capacitance, which was attributed to the extendable active sites of redox reaction.

To explore the realistic application of the rGO/NiCo/PPy composite, CV, GCD, EIS and cycling performance were tested using rGO/NiCo/PPy composite as positive electrode and rGO/PPy as negative electrode in 3M KOH solution.
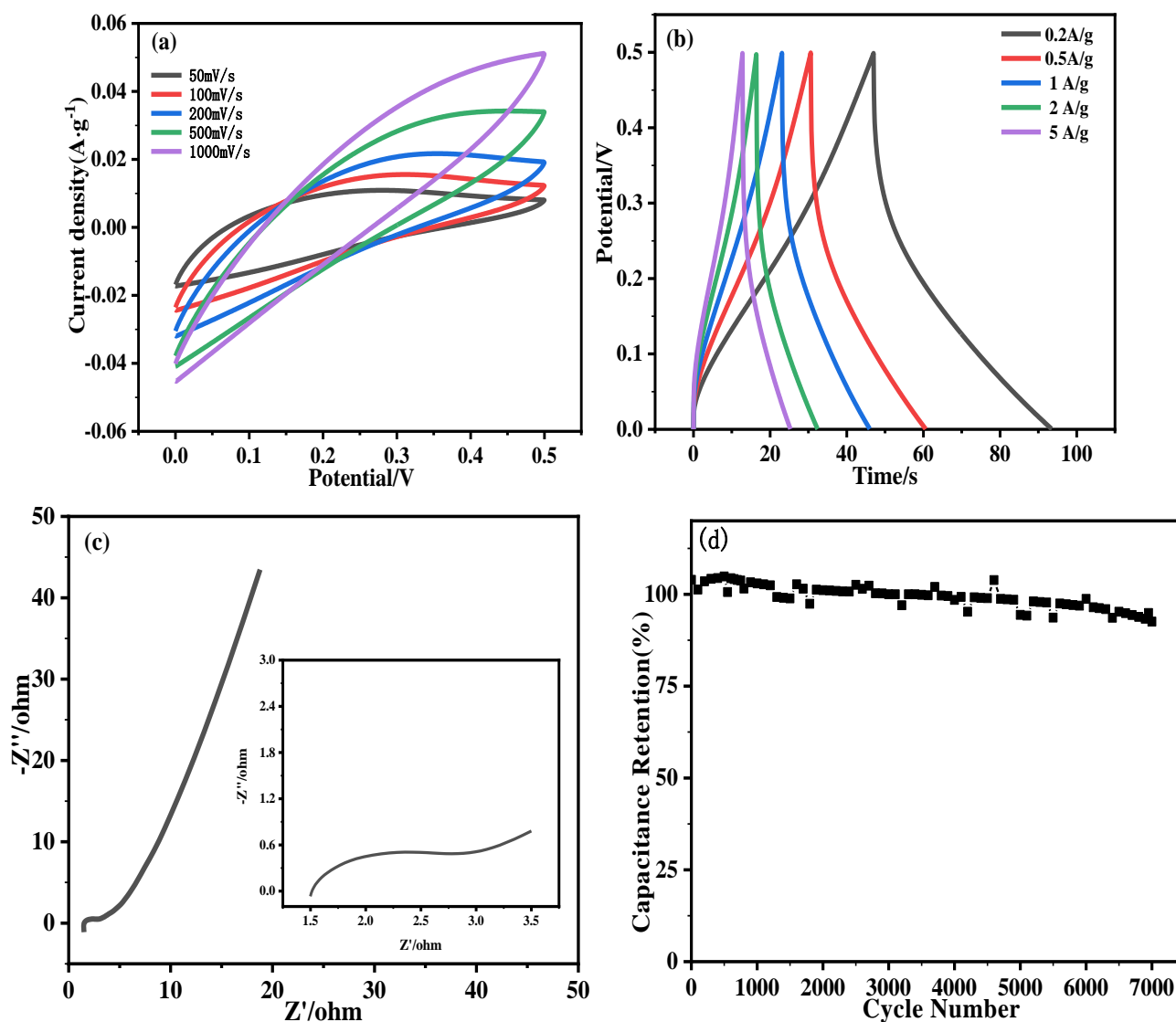
Fig. 6. (a) CV of rGO/NiCo/PPy and rGO/PPy ASC device, (b) GCD of the ASC device at different current densities, (c) EIS of the ASC device, (d)Capacitance retention of the ASC device measured at a current density of 1 A/g (color online)

From the CV diagram in Fig. 6a, it can be seen that the redox peak was basically invisible. It may be that under alkaline conditions, PPy was uniformly and densely covered on the appearance of metal oxide, coupled with negative double electric layer capacitance behavior, and the double electric layer performance was reflected as a whole. Similarly, the GCD diagram in Fig. 6b also proved this

point. The GCD curve was similar to a triangle, which also indicated that the double layer capacitance behavior was the main. The specific capacitances calculated according to formula (1) were 37.4, 60.6, 92, 129.6 and 253 F/g, respectively, at the current densities of 0.2, 0.5, 1, 2, 5 A/g. The EIS diagram of Fig. 6c provided a further understanding of ion diffusion in the material. R_S referred to

the equivalent series resistance, whose value was the intercept with X. The R_S value was 1.49 Ω, which was influenced not only by electronic resistance of electrode material, but also by external factors, namely electrolyte ionic resistance and interface resistance. When the conductivity of the electrode was high and the electrode was well-contacted with the electrolyte, a smaller R_S value will be obtained. In addition, rGO/NiCo/PPy composite possessed high stability as the positive electrode of supercapacitor. As shown in Fig. 6d, the capacity retention rate was approximately 94% after 7000 cycles at 20 mA/cm. As the active material was gradually activated, the capacitance increased slightly during the first 100 cycles. Therefore, the stability of rGO/NiCo/PPy became better and better in redox reaction, and rGO and nickel-cobalt oxide greatly improved the conductivity of the electrode and more active sites for redox reaction, respectively. These results further improved the practical application of rGO/NiCo/PPy described in this work for supercapacitor.

4. Conclusions

In conclusion, rGO/NiCo composite was successfully synthesized by Hummer's method and hydrothermal method, and then further compounded with polypyrrole by in-situ polymerization. Finally, a unique conductive polymer coated with sea urchin-like structure was constructed and the special structure provided guarantee for superior electrochemical characteristics. Among all samples, the specific capacitance of rGO/NiCo/PPy is 333.2 F/g at 1 A/g. Subsequently, rGO/NiCo/PPy was used to prepare asymmetric flexible supercapacitor devices, which also shows good electrochemical performance. The flexible device obtains a specific capacitance of 253 F/g at 5 A/g, and the specific capacitance still remains 94% after 7000 charge and discharge cycles. Its excellent electrochemical performance indicates its application prospect in flexible supercapacitors.

References

[1] J. Xiong, D. Xu, Environ. Res. **194**, 110718 (2021).

[2] Y. Zeng, Y. Cao, X. Qiao, B. C. Seler, Y. Tang, Sci. Total Environ. **663**, 329 (2019).

[3] Z. Zhao, K. Xia, Y. Hou, Q. Zhang, Z. Ye, J. Lu, Chem. Soc. Rev. **50**, 12702 (2021).

[4] D. P. Chatterjee, A. K. Nandi, J. Mater. Chem. A **9**, 15880 (2021).

[5] Y. Wang, X. Wu, Y. Han, T. Li, J. Energy Storage. **42**, 103053 (2021).

[6] G. Xu, P. Nie, H. Dou, B. Ding, X. Zhang, Mater. Today **20**, 191 (2017).

[7] Y. Huang, L. Peng, Y. Liu, G. Zhao, J. Chen, G. Yu, ACS Appl. Mater. Inter. **8**, 15205 (2016).

[8] L. Chen, J. Deng, Y. Song, S. Hong, H. Lian, ChemElectroChem **6**, 5870 (2019).

[9] T. G. Lim, B. T. Ho, J. W. Suk, J. Mater. Chem. A. **9**, 4800 (2021).

[10] M. Jia, S. Geng, Q. Jiang, C. Xu, Y. Zhang, G. Yin, F. Jia, X. Wang, T. Zhou, B. Liu, J. Mater. Sci. **56**, 3911 (2021).

[11] T. Liu, L. Zhang, B. Cheng, J. Yu, Adv. Energy Mater. **9**, 1803900 (2019).

[12] S. Kumar, G. Saeed, L. Zhu, K. N. Hui, N. H. Kim, J. H. Lee, Chem. Eng. J. **403**, 126352 (2021).

[13] L. H. Tseng, P. H. Wang, W. C. Li, C. H. Lin, T. C. Wen, J. Power Sources **516**, 230624 (2021).

[14] D. Y. Wu, W. H. Zhou, L. Y. He, H. Y. Tang, X. H. Xu, Q. S. Ouyang, J. J. Shao, Carbon **160**, 156 (2020).

[15] A. Zaka, K. Hayat, V. Mittal, ACS Appl. Electron. Mater. **3**, 574 (2021).

[16] Z. Li, S. Gadipelli, Y. Yang, G. He, J. Guo, J. Li, Y. Lu, C. A. Howard, D. J. L. Brett, I. P. Parkin, F. Li, Z. Guo, Energy Storage Mater. **17**, 12 (2019).

[17] M. A. Khalily, B. Patil, E. Yilmaz, T. Uyar, Nanoscale **1**, 1224 (2019).

[18] Q. Zhang, D. Gu, H. Li, Z. Xu, H. Sun, J. Li, L. Wang, L. Shen, Electrochim. Acta **367**, 137455 (2021).

[19] A. Zhang, R. Zhao, L. Hu, R. Yang, S. Yao, S. Wang, Z. Yang, Y. M. Yan, Adv. Energy Mater. **11**, 2101412 (2021).

[20] S. Zhu, L. Li, J. Liu, H. T. Wang, F. Dong, ACS Nano **12**, 1033 (2018).

[21] G. Wang, Z. Yan, N. Wang, M. Xiang, Z. Xu, ACS Appl. Nano Mater. **4**, 9034 (2021).

[22] M. Zhang, Y. Xu, H. Fan, N. Zhao, B. Yan, C. Wang, J. Ma, A. K. Yadav, W. Zhang, X. Zheng, M. Li, G. Dong, W. Wang, J. Alloys Compd. **826**, 154115 (2020).

[23] T. Shi, Y. Feng, T. Peng, B. Yuan, Electrochim. Acta **381**, 138245 (2021).

[24] J. Li, J. Ao, C. Zhong, T. Yin, Appl. Surf. Sci. **563**, 150301 (2021).

[25] L. Zhao, S. Lei, Q. Tu, L. Rao, W. Zen, Y. Xiao, B. Cheng, J. Energy Storage. **43**, 103171 (2021).

[26] T. Liu, L. Zhang, W. You, J. Yu, Small **14**, 1702407 (2018).

[27] Y. Jeong, I. Son, S. H. Baek, Appl. Surf. Sci. **467**, 963 (2019).

[28] F. Zhao, D. Zheng, Y. Liu, F. Pan, Q. Deng, C. Qin, Y. Li, Z. Wang, Chem. Eng. J. **415**, 128871 (2021).

[29] R. Zhang, H. Pang, J. Energy Storage **33**, 102037 (2021).

[30] Y. Wang, Y. Ding, X. Guo, G. Yu, Nano Res. **12**, 1978 (2019).

[31] P. Das, S. Mondal, S. Malik, J. Energy Storage **39**, 102662 (2021).

[32] K. Kong, W. Xue, W. Zhu, W. Ye, Z. Zhang, R. Zhao, D. He, J. Power Sources **470**, 228452 (2020).

[33] Y. Diao, H. Chen, Y. Lu, L. M. Santino, H. Wang, J. M. D'Arcy, ACS Appl. Energy Mater. **2**, 3435 (2019).

[34] Q. Liu, J. Qiu, C. Yang, L. Zang, G. Zhang, E. Sakai, Int. J. Energy Res. **44**, 9166 (2020).

[35] Y. K. Kim, K. Y. Shin, Appl. Surf. Sci. **547**, 149141 (2021).

[36] W. Jiang, F. Hu, Q. Yan, X. Wu, Inorg. Chem. Front. **4**, 1642 (2017).

[37] S. Ishaq, M. Moussa, F. Kanwal, R. Ayub, T. N. Van, U. Azhar, D. Losic, Electrochim. Acta **427**, 140883 (2022).

[38] Y. Zhou, J. Li, G. Xiong, X. He, Z. Huang, Y. Wang, Synth. Met. **282**, 116954 (2021).

[39] S. Wei, C. Wan, L. Zhang, X. Liu, W. Tian, J. Su, W. Cheng, Y Wu, Chem. Eng. J. **429**, 132242 (2022).

[40] S. Dhibar, A. Roy, S. Malik, Eur. Polym. J. **120**, 109203 (2019).

[41] M. Dong, Z. Wang, X. Li, H. Guo, J. Wang, G. Yan, Chem. Eng. Sci. **221**, 115709 (2020).

[42] Y. Yang, M. Wang, Z. Shi, R. Xiao, X. Sun, Y. Chen, J. Alloys Compd. **868**, 159128 (2021).

[43] J. Mao, C. He, J. Qi, A. B. Zhang, Y. W. Sui, Y. Z. He, Q. K. Meng, F. X. Wei, J. Electron. Mater. **47**, 471 (2017).

[44] J. Wang, K. Ma, J. Zhang, F. Liu, J. P. Cheng, J. Colloid Interf. Sci. **50**7, 290 (2017).

[45] A. J. Hu, C. Shu, C. Xu, J. Li, J. Long, Chem. Eng. J. **382**, 122854 (2019).

[46] G. Qu, J. Cheng, X. Li, D. Yuan, P. Chen, X. Chen, B. Wang, H. Peng, Adv. Mater. **28**, 3605 (2016).

[47] D. Long, H. Liu, Y. Yuan, J. Li, Z. Li, J. Zhu, J. Alloys Compd. **805**, 1096 (2019).

_____

*Corresponding authors: 6615001@glut.edu.cn, xfan@glut.edu.cn